Precipitation of high Mg-calcite and protodolomite using dead biomass of aerobic halophilic bacteria

Qigao Fan[1, 2], Deng Liu[1, 2, *], Dominic Papineau[1, 3, 4, 5], Xuan Qiu[1], Hongmei Wang[1, 2], Zhenbing She[1] and Linduo Zhao[6]

[1]State Key Laboratory of Biogeology and Environmental Geology, China University of Geosciences, Wuhan 430074, China

[2]School of Environmental Studies, China University of Geosciences, Wuhan 430074, China

[3]London Centre for nanotechnology, University College London and Birkbeck College London, 17-19 Gordon Street, London, UK

[4]Department of Earth Sciences, University College London, London, UK

[5]Center for Planetary Sciences, University College London, London, UK

[6]Illinois Sustainable Technology Center, Prairie Research Institute, University of Illinois at Urbana-Champaign, Champaign, Illinois 61820, USA

Corresponding author:

Deng Liu (liud_cug@126.com)

Revised for *Journal of Earth Science*

October 04, 2020

ABSTRACT

The microbial dolomite model has been used to interpret the origin of sedimentary dolomite. In this model, the formation of low-temperature protodolomite, an important precursor to sedimentary dolomite, can be facilitated either by actively metabolizing cells of anaerobic microbes and aerobic halophilic archaea or by their inactive biomass. Aerobic halophilic bacteria are widely distributed in (proto-)dolomite-depositing evaporitic environments and their biomass might serve as a template for the crystallization of protodolomite. To test this hypothesis, carbonation experiments were conducted using dead biomass of an aerobic halophilic bacterium (*Exiguobacterium* sp. strain JBHLT-3). Our results show that dead biomass of JBHLT-3 can accelerate Mg^{2+} uptake in carbonate mineral precipitates. In addition, the amount of Mg incorporated into Ca-Mg carbonates is proportional to the concentration of biomass. High Mg-calcite is produced with 0.25 or 0.5 g/L biomass, whereas protodolomite forms with 1 g/L biomass. This is confirmed by the main Raman peak of Ca-Mg carbonates, which shifts towards higher wavenumbers with increased Mg substitution. Microbial cells and their imprints are preserved on the surface of high Mg-calcite and protodolomite. Hence, this study furthers our understanding of the dolomitization within buried and dead microbial mats, which provides useful insights into the origin of ancient dolomite.

KEY WORDS: protodolomite, high Mg-calcite, Mg-hydration effect, microbial dead biomass, biosignature

0 INTRODUCTION

Even though the mineral dolomite has been studied for more than two centuries, its genesis is still a topic of ongoing debate in sedimentary geology (Arvidson and Mackenzie, 1999). Dolomite is abundant in the pre-Holocene geological records (Warren, 2000; Wang et al., 2019), yet it rarely precipitates in modern open-ocean water environments (Warren, 2000). Many efforts to synthesize low-temperature dolomite in the laboratory have met with failure (Land, 1998; Xu et al., 2013). Therefore, it is a consensus that dolomite precipitation is controlled by reaction kinetics (Land, 1998; Wright and Wacey, 2005; Kaczmarek and Thornton, 2017; Ngia et al., 2019).

The discovery of Holocene dolomite is normally restricted to evaporitic regimes, such as inland hypersaline lakes and coastal lagoons (Petrash et al., 2017). Interestingly, these dolomites occur predominantly within the microbial mat layer of sediments (Bontognali et al., 2010; Nascimento et al., 2019). In particular, poorly-ordered calcian dolomite (Ca-dolomite) and protodolomite (a dolomite-like mineral with no Ca-Mg ordering) are typically found in the surface microbial mat, while partially-ordered dolomite becomes dominant in the deeper layers (Petrash et al., 2017). These field observations suggest that microorganisms might serve as a possible trigger for the precipitation of Holocene dolomite, and that a protodolomite-to-dolomite transformation took place under early diagenetic conditions (Petrash et al., 2017).

Laboratory studies, mostly based on bench-scale cultivation experiments, have revealed that some types of microbes are able to reduce the low-temperature kinetic barrier to the precipitation of dolomite (e.g., Vasconcelos et al., 1995; van Lith et al., 2003; Roberts et al., 2004; Sánchez-Román et al., 2008; Kenward et al., 2009;

Bontognali et al., 2012). These findings have inspired the establishment and development of so-called microbial dolomite model, which is frequently used to explain the occurrence of Holocene dolomite, and perhaps shed light on the origin of dolomite with a transient distribution during the Phanerozoic but dominant during the Precambrian (McKenzie and Vasconcelos, 2009). Noticeably, a recent argument holds that microbially-mediated dolomite is protodolomite rather than previously presumed ordered dolomite, due to the fact that no visible evidence of ordered-cation arrangement can be found in some X-ray diffraction (XRD) patterns (Gregg et al., 2015). More recently, however, Daye et al. (2019) claimed that ordered and Mn-rich dolomite could precipitate with the aid of anaerobic photosynthetic bacteria. Although protodolomite may be the solid product in the most bioassisted systems, protodolomite is generally considered as an important precursor to ordered dolomite (Rodriguez-Blanco et al., 2015). Therefore, microbial mediation is still a possible pathway for sedimentary dolomite.

In the microbial dolomite model, active microbial metabolism is the key in the precipitation of low-temperature (proto-)dolomite (Vasconcelos et al., 1995; McKenzie and Vasconcelos, 2009). In general, microbial decomposition of organic substrates could raise high pH through ammonification, and high levels of dissolved inorganic carbon in the sediment porewaters. While the latter might counteracts the former, diffusion of alkalinity from seawater overlying sediments likely leads to overall alkaline conditions, adequate for carbonate precipitation. Indeed, these changes can enhance (proto-)dolomite saturation and lead to protodolomite precipitation (Vasconcelos et al.,

1995).

In addition to these processes, Bontognali and co-workers (2010) recently proposed a revised microbial model to interpret the formation of dolomite within buried microbial mats, which showed no signs of microbial activity. According to their model, (proto-)dolomite can nucleate and grow from an over-saturated solution within microbial extracellular polymeric substances (EPS). As such, microbial EPS can behave as a template for (proto-)dolomite crystallization. Subsequent studies further verified the protodolomite-template property of EPS (Bontognali et al., 2014; Liu et al., 2020). Moreover, recent experimental studies showed that the crystallization of protodolomite could also be promoted by inactive microbial biomass of some anaerobic microbes (such as facultative iron-reducing bacteria, sulfate-reducing bacteria and methanogens) and aerobic halophilic archaea (Kenward et al., 2013; Zhang et al., 2015; Qiu et al., 2017; Huang et al., 2019). These observations collectively suggest that non-metabolizing or even dead microbial mats (both EPS and biomass included) should be taken into account as possible trigger factors for (proto-)dolomite formation (Bontognali et al., 2010; Kenward et al., 2013).

Aerobic halophilic bacteria are an important part of microbial biomass of buried and inactive mats in modern (proto-)dolomite depositing environments (Disi et al., 2017). It has been well documented that aerobic halophilic bacteria in active state are capable of triggering protodolomite formation (Sánchez-Román et al., 2008, 2009; Deng et al., 2010; Disi et al., 2017; Alibrahim et al., 2019; Liu et al., 2019a). However, to date, it is still unclear whether their inactive biomass could serve as a template for

protodolomite formation. To achieve this goal, Ca-Mg carbonate crystallization experiments were carried out with dead biomass of *Exiguobacterium* sp. strain JBHLT-3, which is a moderately halophilic aerobic bacterium isolated from a Chinese dolomite-forming lake (Lake Jibuhuangtu Nuur, Inner Mongolia) (Liu et al., 2019a). The new results show that the dead biomass of JBHLT-3 can accelerate the uptake of Mg^{2+} into growing Ca-Mg carbonates, leading to form Mg-calcite and protodolomite.

1 MATERIALS AND METHODS

1.1 Bacterial strain and culture medium

In our previous study, actively metabolizing JBHLT-3 was demonstrated to facilitate protodolomite formation in the presence of proteinaceous substrates, such as peptone (Liu et al., 2019a). The template effect of its dead biomass on the precipitation of protodolomite was further tested in present work. Strain JBHLT-3, which is kept at the State Key Laboratory of Biogeology and Environmental Geology, China University of Geosciences (Wuhan), was cultivated in clear glass flasks containing a saline medium as described by Liu et al. (2019a). Cells of JBHLT-3 were incubated in 500-mL Erlenmeyer flasks at 25 °C and 160 rpm.

1.2 Collection and characterization of dead biomass

The flasks were periodically tested for cell growth by measuring optical density at 600 nm (OD_{600}). Once the bacterial growth reached the late-log phase, the solution of carbonyl cyanide m-chlorophenylhydrazone (CCCP; a powerful metabolic inhibitor for respiration) was added to the flasks to get the final concentration of 1 mM. In doing so,

135 the cells of strain JBHLT-3 were killed but remained intact. The CCCP-treated biomass
136 was collected by centrifugation (7500×g, 10 min). Excess medium and EPS were
137 removed by washing with 5.2% sterile NaCl solution. After washing, cells were re-
138 suspended in aforementioned sterile NaCl solution as a stock solution. A portion of
139 biomass was weighed to determine the concentration of wet biomass. The cell number
140 was determined by acridine-orange direct counting (AODC). In brief, cells of strain
141 JBHLT-3 were deposited onto 0.2 μm GTBP filters (Millipore, USA) and washed three
142 times with 5.2% sterile NaCl solution. After then, cells were stained with acridine
143 orange (0.01%) and counted with a Zeiss Axioplan2 epifluorescence microscope (Carl
144 Zeiss, Germany) using a 100× objective lens (Liu et al., 2011; Wang et al., 2018).
145 The viability of JBHLT-3 cells before and after exposure to CCCP was measured
146 as colony forming units (CFU). Cell suspensions with or without CCCP treatment were
147 plated onto plates of solid saline medium (0.2% agar). The number of CFU was counted
148 visually. Cell suspensions were also characterized by secondary electron imaging in a
149 scanning electron microscopy (SEM) to examine cell morphology upon CCCP
150 treatment. Prior to SEM observations, cells were fixed, dehydrated, critical point dried,
151 and then coated with Pt (Liu et al., 2019a). Images were obtained using a Hitachi
152 SU8010 SEM (Hitachi, Japan) and operating at 5-10 kV, at the State Key Laboratory of
153 Biogeology and Environmental Geology, China University of Geosciences (Wuhan) (Li
154 et al., 2018).
155 A microbial cell surface contains various functional groups and especially
156 carboxyl groups. It has been documented that carboxyl group ($–COO^-$) can facilitate the

157 uptake of Mg^{2+} into Ca-Mg carbonate (Roberts et al., 2013; Qiu et al., 2017). To
158 quantify the concentration of biomass-associated carboxyl group, the pristine and
159 CCCP-treated cells were titrated using a ZEN3600 Zetasizer (Malvern, USA) (Liu et
160 al., 2019a). The Profit 4.1 program was used to model the titration data (Liu et al.,
161 2019a).

162 **1.3 Carbonation experiments with microbial dead biomass**

163 The carbonation experiments were conducted using a NH_4HCO_3 free-drift
164 technique described elsewhere (Lian et al., 2006). In this method, the carbonation
165 driving force, CO_2 and NH_3 gases, were generated by the decomposition of NH_4HCO_3
166 and then slowly diffused into the solution that consisted of cations of Ca^{2+} and Mg^{2+}
167 and different concentrations of CCCP-treated biomass. The dissolution of CO_2 and NH_3
168 could result in the elevation of solution pH and alkalinity. As a result, the solution would
169 gradually become saturated with respect to protodolomite and other carbonates. In
170 general, a series of bacterial suspension was prepared in a number of 100-mL glass
171 flasks, in which $CaCl_2$, $MgCl_2$, and dead cells were added at the desired concentrations.
172 The concentration of $CaCl_2$ and $MgCl_2$ was fixed at 10 mM and 50 mM, respectively,
173 whereas the final wet biomass ranged from 0 to 1 g/L. AODC results revealed that 1
174 g/L wet biomass of JBHLT-3 corresponded to ca. 3×10^8 cells/mL. The flasks were then
175 placed in a closed desiccator containing 15 g of NH_4HCO_3 powders. In the process of
176 precipitation, the desiccator was kept at 25 °C in an incubator. All experiments were
177 performed in duplicate.

178 **1.4 Chemical analyses**

179 The duration of the precipitation experiments lasted two weeks. The solution pH
180 and concentrations of aqueous Mg^{2+} and Ca^{2+} were measured before and after
181 mineralization. Specifically, pH was determined in the supernatants. The
182 concentrations of Ca^{2+} and Mg^{2+} were determined using a Thermofisher ICAP6300
183 inductively coupled plasma-optical emission spectrometry (ICP-OES, Thermo
184 Scientific, USA).

185 **1.5 Mineral analyses**

186 After the 14-day incubation, the precipitates produced were collected and purified.
187 Multiple approaches were employed to characterize solid products. Specifically, prior
188 to X-ray diffraction (XRD) analysis, the samples were re-suspended in a detergent
189 solution consisted of 5% sodium dodecyl sulfate and 5% Triton X-100 to remove
190 organic debris (Liu et al., 2019a). After washing and air-dried, solid products were
191 investigated by a Scintag X1 XRD with Cu Kα radiation (40 kV, 35 mA), at the State
192 Key Laboratory of Geological Processes and Mineral Resources, China University of
193 Geosciences (Wuhan). XRD data analysis was performed by Rietveld refinement using
194 the MDI Jade 6.0 software. The mol-percentage of $MgCO_3$ in Ca-Mg carbonates was
195 calculated from the position of (104) peaks (Bischoff et al., 1983). It has been proposed
196 that the Raman band positions of Ca-Mg carbonates can shift to higher values as a
197 function of Mg substitution (Perrin et al., 2016). To independently confirm this in our
198 samples, an investigation was done using a laser Raman microscope system (RM-1000;
199 Renishaw, UK) (Liu et al., 2020).

200 The morphology and chemical composition of solid precipitates were

characterized by SEM with energy dispersive spectroscopy (EDS; Oxford Instruments XMax 80, UK). Samples were Pt-coated prior to SEM observations. Because our carbonate samples were relatively thick, their interior microstructures could not be easily captured by conventional transmission electron microscopy (TEM). Hence, focused ion beam (FIB) technique was utilized to prepare ultrathin sections of samples for TEM investigations. The thin sections were deposited on carbon-coated TEM copper grids. TEM observations in bright field imaging mode and selected area electron diffraction (SAED) were performed with an FEI Talos F200X microscope with a 200 kV accelerating voltage, at the Center for Materials Research and Analysis, Wuhan University of Technology.

The incorporation of Mg^{2+} ions into calcitic structure produces various precipitates, including low Mg-calcite (< 4 mol% $MgCO_3$), high Mg-calcite (with 4-36 mol% $MgCO_3$), protodolomite (with more than 36 mol% and up to ca. 55 mol% $MgCO_3$ but with no Ca-Mg order) and dolomite (Zhang et al., 2015). These Mg-contents were employed to categorize our Ca-Mg carbonates.

2 RESULTS

2.1 Microbial activity, morphology and surface chemistry upon CCCP treatment

Enumeration data show that the fresh culture density is 2×10^8 CFU/mL. In contrast, there is no colony formation in the presence of CCCP, which indicates that 1 mM concentration of CCCP is sufficient to kill these cells. SEM observations reveal that the strain JBHLT-3 is a rod-shaped bacillus (Fig. 1A and B) and that cells remain intact

after CCCP treatment (Fig. 1C and D). Our titration results indicate that dead biomass of JBHLT-3 has a carboxyl concentration of 1.5×10^{-3} mol/g, close to the value estimated from pristine cells (1.7×10^{-3} mol/g). These titration data demonstrate that CCCP treatment has negligible impact on the concentrations of surface-bound carboxyl group.

2.2 Changes of chemical parameters as a result of carbonation

The effect of biomass on the aqueous chemistry of carbonate mineral formation is evaluated with dead JBHLT-3 cells at 0-1 g/L wet biomass. By the end of 14-days incubation, the sublimation-decomposition of solid NH_4HCO_3 has fully taken place, and a strong odor of gaseous ammonia is detected in the desiccator. As a consequence of ammonia dissolution, a significant rise in pH is observed for each flask (Table 1). The pH increases from ca. 7.00 to 9.27, 9.15, 9.11, and 9.06 in the systems amended with 0, 0.25, 0.5 and 1 g/L biomass, respectively. Additionally, along with the diffusion of CO_2 from NH_4HCO_3 sublimation, the Ca^{2+} ions concentration in solution decreases to ca. 0 mM in all groups (Table 1). Unlike Ca^{2+} ions, large differences in the change of Mg^{2+} concentration are found among mineralization systems. The concentration of Mg^{2+} in the biomass-free experiments exhibits negligible changes, whereas it declines when biomass is introduced into experimental solutions (Table 1). The removal of Mg^{2+} from the solution in the biomass-containing systems might be caused by the incorporation of Mg^{2+} into growing Ca-Mg carbonates and/or the adsorption of Mg^{2+} onto microbial biomass. Moreover, the experiments apparently show that these Mg^{2+} decreases are related to the increased biomass concentration in solution.

2.3 XRD results

The XRD pattern of crystals from biomass-free systems exhibits only sharp aragonite ($CaCO_3$) reflections, indicating the formation of pure aragonite (Fig. 2A). However, as evidenced by the appearance of XRD reflections corresponding to the rhombohedral structure, Ca-Mg carbonates predominantly occur in the systems with biomass (Fig. 2B-D). Examination of the strongest reflection (104) shows a shift towards higher values of full widths at half maximum (FWHM) and higher 2θ values (corresponding to lower values of *d*-spacing) and with increasing concentration of biomass (Fig. 2 and Fig. 3A). The average $MgCO_3$ content in Ca-Mg carbonates is estimated from the (104) peak-shift method (Bischoff et al., 1983). The results show that the Ca-Mg carbonates with 15.4, 25.6 and 44.2 mol% $MgCO_3$ precipitate from the systems with 0.25, 0.5 and 1 g/L biomass, respectively (Table 1 and Fig. 3B). Furthermore, a positive linear relationship between the concentration of biomass and the mol-percentage of $MgCO_3$ in Ca-Mg carbonates is observed (Fig. 3B). Accordingly with the terminology defined earlier, the precipitated Ca-Mg carbonates in the experimental solutions with 0.25 and 0.5 g/L biomass are high Mg-calcite. Whereas, the carbonate precipitated in the presence of 1 g/L biomass is identified as protodolomite, based on its near-dolomite stoichiometry, and the lack of ordering reflections in the XRD pattern, such as (003), (015) and (021) (Fig. 2D).

2.4 Raman data

The resulting Ca-Mg carbonates are further characterized by Raman spectroscopy in the range of 100-1200 cm^{-1}. As shown in Fig. 4A, the Raman spectra of all the samples have a comparable pattern of peaks that indicate a similar atomic structure.

267 According to published literature, these Raman bands can be assigned to translational
268 external mode (T), librational external mode (L), and two internal vibrations (ν1 and
269 ν4) (Perrin et al., 2016). However, the bands shift to higher wavenumbers with
270 increasing concentrations of biomass (Fig. 4A). Combining our data with previously
271 published data sets (Edwards et al., 2005; Perrin et al., 2016), a clear positive correlation
272 is shown between peak positions for each mode and Mg content (Fig. 4B-E).

273 **2.5 SEM observations**

274 Secondary electron images reveal that the crystals from biomass-containing
275 systems are spherical in shape and the diameter of these spherulites is generally 10 to
276 15 μm, regardless of the dosage of biomass used (Fig. 5). As evidenced by EDS, the
277 $MgCO_3$ content (i.e., the ratio of Mg Kα/Ca Kα) is 14.7, 26.2 and 44.8 mol% for the
278 solid products precipitated from solutions with 0.25, 0.5 and 1 g/L biomass,
279 respectively (Fig. 5A-B and D). These data are consistent with the XRD results (Fig.
280 2). It is interesting to note that cells of JBHLT-3 or their imprints are also found on the
281 surface of carbonate spherulites. High-magnification secondary electron images show
282 that protodolomite precipitates have a rather rough surface, due to the presence of cells
283 and numerous nanocrystals (Fig. 5E-G).

284 **2.6 TEM observations**

285 The crystal structure of Ca-Mg carbonate precipitates is examined in detail by
286 TEM (Fig. 6). The Mg-calcite produced in the reactors either with 0.25 or 0.5 g/L
287 biomass is composed of randomly-distributed nano-crystals (Fig. 6A and C). The
288 distinguishable lattice fringe spacing is 2.993 Å for the sample from the systems with

289 0.25 g/L biomass (Fig. 6B), and 2.961 Å for the phase formed in 0.5 g/L biomass-
290 amended systems (Fig. 6D). These values are consistent with the (104) plane of Mg-
291 calcite. Similarly to Mg-calcites, our protodolomite is composed of numerous
292 nanoscopic grains (Fig. 6E). High-resolution TEM images further indicate that its (104)
293 *d*-spacing is around 2.910 Å (Fig. 6F). In agreement with XRD data, our SAED results
294 confirm the disordered structure of protodolomite, because of the lack of superlattice
295 reflections expected from ordered-dolomite [e.g., (003), (015) and (021)] (Fig. 6F).
296

297 **3 DISCUSSION**

298 Aragonite (a Mg-free carbonate), rather than Ca-Mg carbonates, is the favored
299 product in our biomass-free sets, regardless of sufficient Mg source therein. Similar
300 observations have been made in other Mg-rich and inorganic systems (e.g., Zhang et
301 al., 2012; Qiu et al., 2017, 2019; Liu et al., 2019a, 2020). It is a consensus that the Mg-
302 hydration is the key kinetic barrier to the formation of Ca-Mg carbonates under ambient
303 conditions (Romanek et al., 2009; Zhang et al., 2012; Shen et al., 2015).

304 When Ca^{2+} and Mg^{2+} ions are dissolved into bulk water, they preferentially bind
305 to water molecules, which leads to the formation of $M(H_2O)_n^{2+}$ clusters (M: Ca or Mg;
306 n: water coordination number) (Romanek et al., 2009). However, it has been well
307 documented that the water-exchange kinetics around Ca^{2+} and Mg^{2+} ions are
308 significantly different (Jiao et al., 2006). For instance, the lifetime of water molecules
309 in the outer hydration shell around Mg^{2+} is hundreds of times longer than that of Ca^{2+}
310 (Jiao et al., 2006). Moreover, the hydration energy of Mg^{2+} under standard condition is

311 also larger than that of Ca^{2+} (1926 kJ per mole vs. 1579 kJ per mole) (Slaughter and
312 Hill, 1991). These results indicate that the dehydration of Mg^{2+}-H_2O clusters is more
313 difficult to achieve compared with Ca^{2+}-H_2O complexes. As such, the strong Mg^{2+}-H_2O
314 associations hinder the interaction of CO_3^{2-} ions with Mg^{2+} ions, and thereby inhibit the
315 incorporation of Mg^{2+} into growing carbonate crystals (Shen et al., 2015). Hence, Mg-
316 hydration effect is likely a major cause for the difficulty in precipitating Ca-Mg
317 carbonates from modern seawater or our biomass-free system, both of which have the
318 Mg/Ca molar ratio as high as 5.0.

319 However, evidence has accumulated showing that Ca-Mg carbonate becomes the
320 predominant phase with aid of actively metabolizing microorganisms (e.g.,
321 Vasconcelos et al., 1995; Sánchez-Román et al., 2008; Deng et al., 2010; Liu et al.,
322 2019a). In this study, data demonstrate that the precipitation of Ca-Mg carbonates is a
323 product catalyzed by dead biomass from an aerobic halophilic bacterium (JBHLT-3),
324 consistent to the emerging view that inactive biomass can serve as template for the
325 nucleation of Ca-Mg carbonates (Kenward et al., 2013; Zhang et al., 2015; Qiu et al.,
326 2017; Huang et al., 2019).

327 According to published literature, the metal-chelation model is likely a mechanism
328 for diminishing the Mg-hydration effect by inactive biomass (Kenward et al., 2013;
329 Huang et al., 2019). Arising from the presence of acid functional groups (e.g., carboxyl)
330 on the microbial cell surface, the negatively-charged microbial biomass provides strong
331 binding sites for cation adsorption onto cell surface (Huang et al., 2019). Upon
332 adsorption, a least one water molecule surrounding Mg^{2+} ions can be replaced by

biomass-associated functional groups (Kenward et al., 2013). It has thus been proposed that these organic-bound Mg-H_2O complexes (especially carboxyl-Mg-H_2O clusters) require lower activation energy for carbonation (Roberts et al., 2013). In doing so, a thin Ca-Mg carbonate layer can be created on the surface of microbial cells and its growth would proceed as long as the saturation condition is maintained. Such template effect of microbial biomass on precipitation of Ca-Mg carbonates is supported by our SEM observations (Fig. 5C &E).

Even though high Mg-calcite has been commonly found in bio-precipitation experiments using various types of microbes, the occurrence of protodolomite (>36 mol% $MgCO_3$) in these systems is rare. As such, it has been suggested that the ability to mediate protodolomite formation is perhaps restricted to specific species (Bontognali et al., 2012). In this study, the increasing uptake of Mg^{2+} in Ca-Mg carbonate precipitates is observed when elevated biomass additives are present in the solution (Fig. 3B), which suggests that the formation of protodolomite is dependent on the concentration of biomass. Such phenomena may be interpreted as arising from the unequal affinity of biomass-associated carboxyl for Ca and Mg adsorption. Specifically, in a biomass-deficient system, Ca^{2+} and Mg^{2+} ions can compete for carboxyl sites. In comparison to Mg^{2+} ion, however, carboxyl group exhibits a greater binding affinity towards Ca^{2+} (Wang et al., 2009). Therefore, Mg-calcite rather than protodolomite is the favored bio-precipitate in most of aforementioned cases. Our titration data indicate that the inactive biomass of JBHLT-3 is rich in carboxyl groups. Once larger amount of JBHLT-3 biomass (corresponding to higher density of carboxyl groups) is introduced

into the precipitation solution, there should be more sufficient binding sites for both Ca and Mg. In this regard, it is possible that microbial biomass carries equal molar concentration of complexed Ca^{2+} and Mg^{2+}, inducing carbonation and protodolomite precipitation.

Such biomass-catalyzed dolomite model can offer a possible route to some Holocene (proto-)dolomites found within buried and dead microbial mats, like the ones in the coastal sabkha of Abu Dhabi, UAE (Bontognali et al., 2010). The strong evaporation in these saline regimes can concentrate the sediment porewaters and perhaps create supersaturation for (proto-)dolomite. Dead microbial biomass, together with EPS, is effective in overcoming the dehydration barrier for Mg^{2+}/Ca^{2+} ions so that the electrostatic force of attraction between these cations and CO_3^{2-} ions increases. Hence, the crystallization of protodolomite could take place within buried and dead microbial mats (Fig. 7).

Our microscopic observations indicate that the produced protodolomite occurs as closely packed aggregates of nanocystals (Figs. 5G & 6E), a typical characteristic of the so-called mesocrystal phase (Cölfen and Antonietti, 2005). Actually, such crystallization behavior has been observed for protodolomite produced by other micorbes (e.g., Bontognali et al., 2008; Sánchez-Román et al., 2008; Liu et al., 2019a). This indicates that microbially-mediated protodolomite might grow through an orientated-attachment mechanism. As mesocrystals are thermodynamically unstable (Cölfen and Antonietti, 2005), they tend to reach equilibrium by converting into more stable phase over time. Specifically for protodolomite, it would transform to crystalline

dolomite during burial diagenesis (Malone et al., 1996). In addition, SEM results show that the presence of bacterial cells on the surface of protodolomite spherulites up to about 15 μm in diameter, smaller than diagenetically produced siderite spheroids (Kölher et al., 2013), diagenetic rosettes of apatite, organic matter and quartz in late Paleoproterozoic stromatolitic phosphorite (Papineau et al., 2016) of ferroan calcite, hematite, and quartz in Eoarchean and Ordovician jasper (Grenne and Slack, 2003; Dodd et al., 2017). However, the new spherulites documented here are morphologically comparable to some abiotic colloids of protodolomite (Rodriguez-Blanco et al., 2015; Liu et al., 2019b) and witherite (Rouillard et al., 2018). Hence, the spherical structure may not be employed as a biosignature for microbially-mediated (proto-)dolomites.

4 CONCLUSIONS

Our laboratory experiments show that the uptake of Mg^{2+} in Ca-Mg carbonate minerals can be facilitated by inactive biomass of an aerobic halophilic bacterium (strain JBHLT-3). Contrary to aragonite formed in the biomass-free systems, high Mg-calcite is the favored product in the experiment systems with either 0.25 or 0.5 g/L of dead biomass, and protodolomite becomes predominant when the dead biomass increases up to 1 g/L. The resulting high Mg-calcite and protodolomite occur as micron-sized spherulites, smaller than known sedimentological spheroids found in Phanerozoic and Precambrian sedimentary rocks, but similar in shape and size to other abiotic spheroids of witherite and silica, also precipitated from alkaline solutions. The protodolomite spherulites are composed of numerous randomly-oriented nano-crystals.

These results are consistent with the emerging view that inactive biomass can function as a template for crystallization of protodolomite, which have important implications for the occurrence of modern dolomite in evaporitic settings.

ACKNOWLEDGMENTS

This work was jointly supported by the National Natural Science Foundation of China (Nos. 41772362 and 41572323), the Strategic Priority Research Program of Chinese Academy of Sciences (No. XDB26000000), the 111 Project of China (No. BP0820004), and the Fundamental Research Funds for the Central Universities, China University of Geosciences (Wuhan) (No. CUGCJ1703). We thank three anonymous reviewers for improving the quality of the manuscript.

REFERENCES CITED

Alibrahim, A., Al-Gharabally, D., Mahmoud, H., Dittrich, M., 2019. Proto-dolomite formation in microbial consortia dominated by *Halomonas* strains. *Extremphiles*, 23: 765-781.

Arvidson, R. S., Mackenzie, F. T., 1999. The dolomite problem: control of precipitation kinetics by temperature and saturation state. *American Journal of Science*, 299: 257-288.

Bischoff, W. D., Bishop, F. C., Mackenzie, F. T., 1983. Biogenically produced magnesian calcite: inhomogeneities in chemical and physical properties; comparison with synthetic phases. *American Mineralogist*, 68: 1183-1188.

421 Bontognali, T. R. R., Vasconcelos, C., Warthmann, R. J., et al., 2010. Dolomite
422 formation within microbial mats in the coastal sabkha of Abu Dhabi (United
423 Arab Emirates). *Sedimentology*, 57: 824-844.
424 Bontognali, T. R. R., Vasconcelos, C., Warthmann, R. J., et al., 2012. Dolomite-
425 mediating bacterium isolated from the sabkha of Abu Dhabi (UAE). *Terra Nova*,
426 24: 248-254.
427 Bontognali, T.R.R., McKenzie, J.A., Warthmann, R.J., et al., 2014. Microbially
428 influenced formation of Mg-calcite and Ca-dolomite in the presence of
429 exopolymeric substances produced by sulphate-reducing bacteria. *Terra Nova*,
430 26: 72-77.
431 Deng, S., Dong, H., Lv, G., et al., 2010. Microbial dolomite precipitation using sulfate
432 reducing and halophilic bacteria: Results from Qinghai Lake, Tibetan Plateau,
433 NW China. *Chemical Geology*, 278: 151-159.
434 Disi, Z. A. A., Jaous, S., Bontognali, T. R. R., et al., 2017. Evidence of a role for aerobic
435 bacteria in high magnesium carbonate formation in the evaporitic environment
436 of Dohat Faishakh Sabkha in Qatar. *Frontiers in Envrionmental Science*, 5: 1.
437 Dodd, M. S., Papineau, D., Grenne, T., et al., 2017. Evidence for early life in Earth's
438 oldest hydrothermal vent precipitates. *Nature*, 543: 60-64.
439 Edwards, H. G. M., Villar, S. E. J., et al., 2005. FT-Raman spectroscopic study of
440 calcium-rich carbonate minerals. *Spectrochimica Acta Part A*, 61: 2273-2280.
441 Gregg, J. M., Bish, D. L., Kaczmarek, S. E., et al., 2015. Mineralogy, nucleation and
442 growth of dolomite in the laboratory and sedimentary environment: a review.

443 *Sedimentology*, 62: 1749-1769.
444 Grenne, T., Slack, J. F., 2003. Bedded jaspers of the Ordovician Lokken ophiolite,
445 Norway: seafloor deposition and diagenetic maturation of hydrothermal plume-
446 derived silica-iron gels. *Mineralium Deposita*, 38: 625-639.
447 Huang, Y., Yao, Q., Li, H., et al., 2019. Aerobically incubated bacterial biomass-
448 promoted formation of disordered dolomite and implication for dolomite
449 formation. *Chemical Geology*, 523: 19-30.
450 Jiao, D., King, C., Grossfield, A., et al., 2006. Simulation of Ca^{2+} and Mg^{2+} solvation
451 using polarizable atomic multipole potential. *Journal of Physical Chemistry B*,
452 110: 18553-18559.
453 Kaczmarek, S. E., Thornton, B. P., 2017. The effect of temperature on stoichiomety,
454 cation ordering, and reaction rate in high-temperature dolomitization
455 experiments. *Chemical Geology*, 468: 32-41.
456 Kenward, P., Goldstein, R., Gonzalez, L., et al., 2009. Precipitation of low-temperature
457 dolomite from an anaerobic microbial consortium: the role of methanogenic
458 Archaea. *Geobiology*, 7: 556-565.
459 Kenward, P. A., Fowle, D. A., Goldstein, R. H., et al., 2013. Ordered low-temperature
460 dolomite mediated by carboxyl-group density of microbial cell walls. *AAPG*
461 *Bulletin*, 97: 2113-2125.
462 Land, L. S., 1998. Failure to precipitate dolomite at 25°C from dilute solution despite
463 1000-fold oversaturation after 32 years. *Aquatic Geochemistry*, 4: 361-368.
464 Li, Y., Zhao, L., Li, Z., et al., 2018. Petrology of garnet amphibolites from the Hualong

Group: Implications for metamorphic evolution of the Qilian Orogen, NW China. *Journal of Earth Science*, 29(5): 1102-1115.

Lian, B., Hu, Q., Chen, J., et al., 2006. Carbonate biomineralization induced by soil bacterium Bacillus megaterium. *Geochimica et Cosmochimica Acta*, 70: 5522-5535.

Liu, D., Yu, N., Papineau, D., et al., 2019a. The catalytic role of planktonic aerobic heterotrophic bacteria in protodolomite formation: Results from Lake Jibuhulangtu Nuur, Inner Mogolia, China. *Geochimica et Cosmochimica Acta*, 263: 31-49.

Liu, D., Xu, Y., Papineau, D., et al., 2019b. Experimental evidence for abiotic formation of low-temperature proto-dolomite facilitated by clay minerals. *Geochimica et Cosmochimica Acta*, 247: 83-95.

Liu, D., Fan, Q., Papineau, D., et al., 2020. Precipitation of protodolomite facilitated by sulfate-reducing bacteria: The role of capsule extracellular polymeric substances. *Chem. Geol.*, 533: 119415.

Malone, M. J., Baker P. A., Burns S. J., 1996. Recrystallization of dolomite: An experimental study from. *Geochimica et Cosmochimica Acta*, 60(12): 2189-2207.

McKenzie, J. A., Vasconcelos, C., 2009. Dolomite Mountains and the origin of the dolomite rock of which they mainly consist: historical developments and new perspectives. *Sedimentology*, 56: 205-219.

Nascimento, G.S., Eglinton, T. I., Haghipour, N., et al., 2019. Oceanographic and

487 sedimentological infuences on carbonate geochemistry and mineralogy in
488 hypersaline coastal lagoons, Rio de Janeiro State, Brazil. *Limnology and*
489 *Oceanography*, 64: 2605-2620.
490 Ngia, N. R., Hu, M., Gao, D., et al., 2019. Application of stable strontium isotope
491 geochemistry and fluid inclusion microthermometry to studies of dolomitization
492 of the deeply buried Cambrain carbonate successions in West-Central Tarim
493 Basin, NW China. *Journal of Earth Science*, 30(1): 176-193.
494 Papineau, D., De Gregorio, B., Fearn, S., et al., 2016. Nanoscale petrographic and
495 geochemical insights on the origin of the Palaeoproterozoic stromatolitic
496 phosphorites from Aravalli Supergroup, India. *Geobiology*, 14: 3-32.
497 Perri, E., Tucker, M., 2007. Bacterial fossils and microbial dolomite in Triassic
498 stromatolites. *Geology*, 35: 207-210.
499 Petrash, D. A., Bialik, O. M., Bontognali, T. R. R., et al., 2017. Microbially catalyzed
500 dolomite formation: From near-surface to burial. *Earth-Science Reviews*, 171:
501 558-582.
502 Qiu, X., Wang, H., Yao, Y., et al., 2017. High salinity facilitates dolomite precipitation
503 mediated by *Haloferax volcanii* DS52. *Earth and Planetary Science Letters*,
504 472: 197-205.
505 Roberts, J. A., Bennett, P. C., González, L. A., et al., 2004. Microbial precipitation of
506 dolomite in methanogenic groundwater. *Geology*, 32: 277-280.
507 Roberts, J. A., Kenward, P. A., Fowle, D. A., et al., 2013. Surface chemistry allows for
508 abiotic precipitation of dolomite at low temperature. *Proceedings of the*

509 *National Academy of Sciences of the United States of America*, 110: 14540-
510 14545.
511 Rodriguez-Blanco, J. D., Shaw, S., Benning, L. G., 2015. A route for the direct
512 crystallization of dolomite. *American Mineralogist*, 100: 1172-1181.
513 Romanek, C.S., Jiménez-López, C., Navarro, A. R., et al., 2009. Inorganic synthesis of
514 Fe-Ca-Mg carbonates at low temperature. *Geochimica et Cosmochimica Acta*,
515 73: 5361-5376.
516 Rouillard, J., García-Ruiz, J.M., Gong, J., et al., 2018. A morphogram for silica-
517 witherite biomorphs and its application to microfossil identification in the early
518 earth rock record. *Geobiology*, 16(3): 279-296.
519 Sánchez-Román, M., Vasconcelos, C., Schmid, T., et al., 2008. Aerobic microbial
520 dolomite at the nanometer scale: Implications for the geologic record. *Geology*,
521 36: 879-882.
522 Sánchez-Román, M., McKenzie, J. A., Wagener, A. D. L. R., et al., 2009. Presence of
523 sulfate does not inhibit low-temperature dolomite precipitation. *Earth and*
524 *Planetary Science Letters*, 285: 131-139.
525 Shen, Z., Brown, P. E., Szlufarska, I., et al., 2015. Investigation of the role of
526 polysaccharide in the dolomite growth at low temperature by using atomistic
527 simulations. *Langmuir*, 31: 10435-10442.
528 Slaughter, M., Hill, R., 1991. The influence of organic matter in organogenic
529 dolomitization. *Journal of Sedimentary Petrology*, 61: 296-303.
530 van Lith, Y., Warthmann, R., Vasconcelos, C., et al., 2003. Sulphate-reducing bacteria

induce low-temperature Ca-dolomite and high Mg-calcite formation. *Geobiology*, 1(1): 71-79.

Vasconcelos, C., McKenzie, J. A., Bernasconi, S., et al., 1995. Microbial mediation as a possible mechanism for natural dolomite formation at low temperatures. *Nature*, 377: 220-222.

Wang, D., Wallace, A. F., De Yoreo, J. J., et al., 2009. Carboxylated molecules regulate magnesium content of amorphous calcium carbonates during calcification. *Proceedings of the National Academy of Sciences of the United States of America*, 106: 21511-21516.

Wang, R., Wang, H., Xiang, X., et al., 2018. Temporal and spatial variations of microbial carbon utilization in water bodies from the Dajiuhu Peatland, Cetral China. *Journal of Earth Science*, 29(4): 969-976.

Wang, X., Xu, X., Ye, Y., et al., 2019. In-situ high-temperature XRD and FTIR for calcite, dolomite and magnesite: Anharmonic contribution to the thermodynamic properties. *Journal of Earth Science*, 30(5): 964-976.

Warren, J., 2000. Dolomite: occurrence, evolution and economically important associations. *Earth-Science Reviews*, 52: 1-81.

Wright, D. T., Wacey, D., 2005. Precipitation of dolomite using sulphate-reducing bacteria from the Coorong Region, South Australia: significance and implications. *Sedimentology,* 52: 987-1008.

Xu, J., Yan, C., Zhang, F., et al., 2013. Testing the cation-hydration effect on the crystallization of Ca-Mg-CO_3 systems. *Proceedings of the National Academy*

553 *of Sciences of the United States of America*, 110: 17750-17755.
554 Zhang, F., Xu, H., Konishi, H., et al., 2012. Polysaccharide-catalyzed nucleation and
555 growth of disordered dolomite: A potential precursor of sedimentary dolomite.
556 *American Mineralogist*, 97: 556-567.
557 Zhang, F., Xu, H., Shelobolina, E. S., et al., 2015. The catalytic effect of bound
558 extracellular polymeric substances excreted by anaerobic microorganisms on
559 Ca-Mg carbonate precipitation: Implications for the "dolomite problem".
560 *American Mineralogist*, 100: 483-494.

Table 1

Geochemical conditions employed in the carbonation experiments with and without biomass and mineral compositions of carbonates.

Experimental set	Before carbonation			After 14-day carbonation						
	pH	Ca^{2+} (mM)	Mg^{2+} (mM)	pH	Ca^{2+} (mM)	Mg^{2+} (mM)	Precipitated Ca (mM) [a]	Precipitated Mg (mM) [a]	Major mineral phase	$MgCO_3$ (mol%) [b]
without biomass	7.02±0.01	9.97±0.07	50.65±0.01	9.27±0.04	0.16±0.05	50.34±0.02	9.81	0.31	aragonite	\
with 0.25 g/L biomass	7.02±0.01	9.95±0.01	50.13±0.01	9.15±0.05	0.23±0.01	48.38±0.07	9.72	1.75	high-Mg calcite	15.4
with 0.5 g/L biomass	7.01±0.01	10.06±0.01	50.09±0.03	9.11±0.04	0.31±0.04	46.69±0.03	9.75	3.40	high-Mg calcite	25.6
with 1 g/L biomass	7.02±0.01	10.02±0.04	50.26±0.01	9.06±0.02	0.25±0.02	42.47±0.05	9.77	7.79	protodolomite	44.2

[a] The precipitated Ca and Mg were calculated as the differences of ion concentration in solution before and after carbonation.

[b] The mole percentage of $MgCO_3$ in Ca-Mg carbonates was calculated from the position of (104) peak using the Bischoff et al. (1983) curve.

Figure caption:

Figure 1. SEM images of strain JBHLT-3 without (A-B) and with (C-D) CCCP treatments.

Figure 2. Rietveld refined XRD patterns of carbonate minerals in the systems with 0, 0.25, 0.5 and 1 g/L inactive biomass, respectively (A: aragonite). The grey line in each panel shows residue (differences between experimental and calculated data). The inset at the top-right for each panel shows (104) peak of Ca-Mg carbonates.

Figure 3. (A) Plots showing the relationship between the concentration of biomass in the systems and FWHM of (104) for Ca-Mg carbonates; (B) Linear correlation between the concentration of biomass and Mg content in carbonate minerals.

Figure 4. (A) Raman spectra of Ca-Mg carbonates produced in the presence of dead biomass. (B-E) Wavenumber of different Raman bands of Ca-Mg carbonates as a function of Mg content.

Figure 5. SEM images and EDS compositions of Ca-Mg carbonates produced with different concentrations of biomass: (A) 0.25 g/L; (B-C) 0.5 g/L; (D-G) 1 g/L. The arrows shown in the panel C indicate the bacterial imprints.

Figure 6. Low-magnification and high-resolution TEM images of Ca-Mg carbonates

obtained in the reactors with different biomass dosages: (A-B) 0.25 g/L; (C-D) 0.5 g/L; (E-F) 1 g/L. The inset SAED pattern shown in panel confirms the disordered structure of protodolomite.

Figure 7. Proposed model illustrating the template effect of buried microbial mats on the formtion of protodolomite.

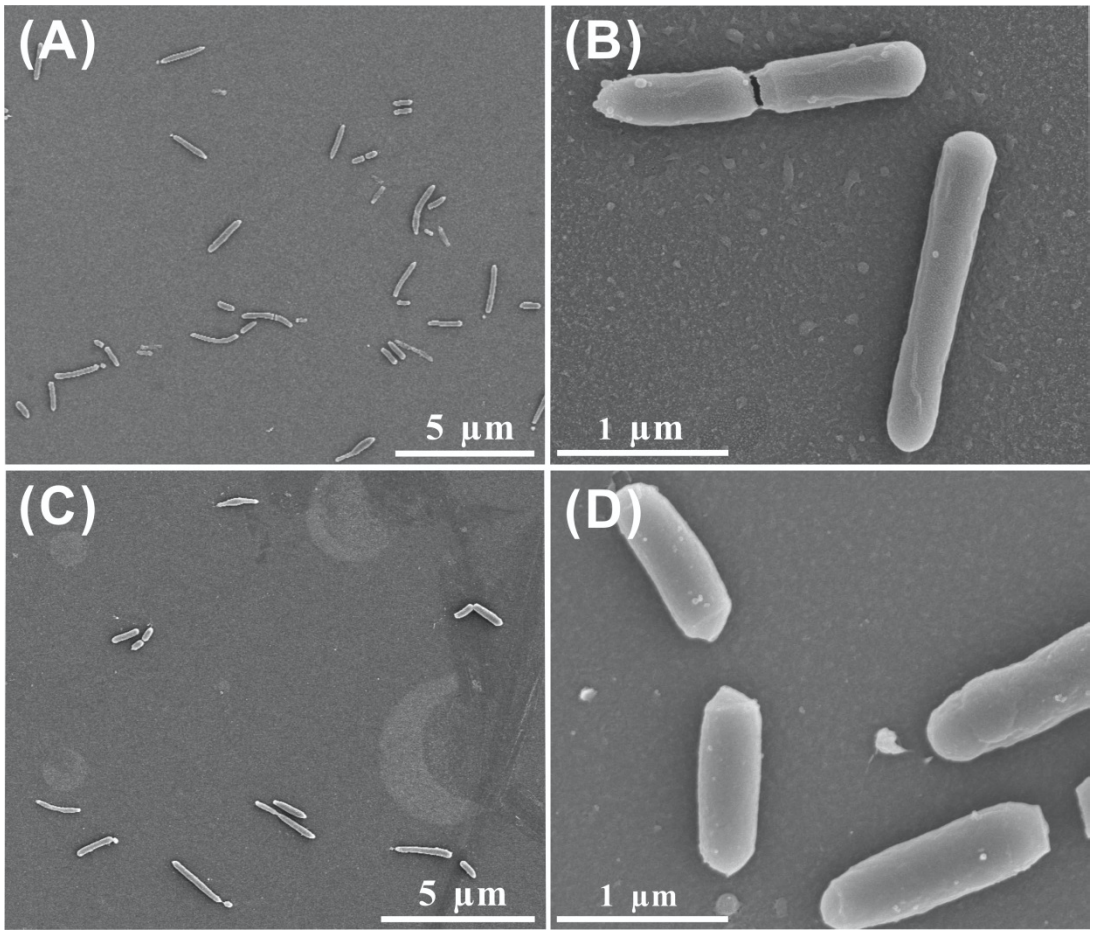

Figure 1

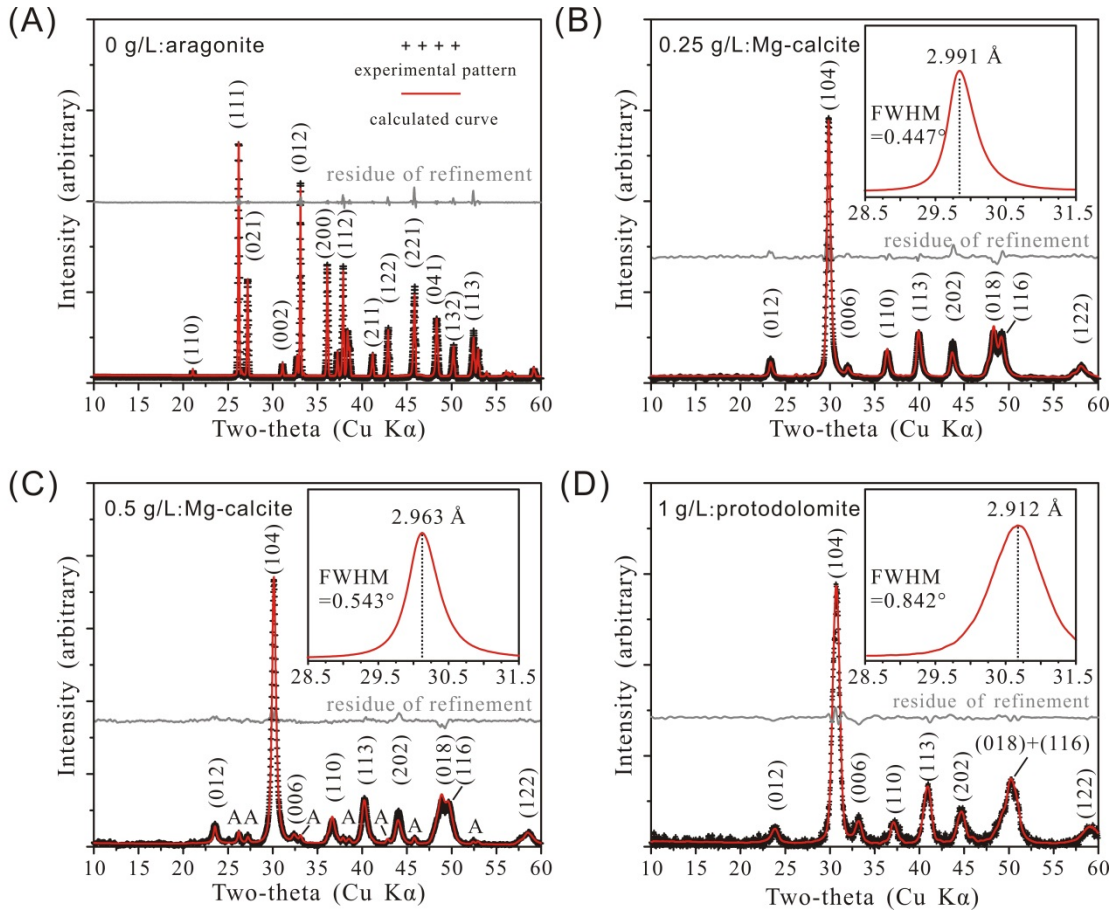
(A)
0 g/L:aragonite
experimental pattern
calculated curve
residue of refinement
(110)
(111)
(021)
(012)
(002)
(200)
(112)
(211)
(122)
(221)
(041)
(132)
(113)
Intensity (arbitrary)
Two-theta (Cu Kα)
(B)
0.25 g/L:Mg-calcite
2.991 Å
FWHM
=0.447°
residue of refinement
(012)
(104)
(006)
(110)
(113)
(202)
(018)
(116)
(122)
(C)
0.5 g/L:Mg-calcite
2.963 Å
FWHM
=0.543°
residue of refinement
(012)
(104)
(006)
(110)
(113)
(202)
(018)
(116)
(122)
A
(D)
1 g/L:protodolomite
2.912 Å
FWHM
=0.842°
residue of refinement
(012)
(104)
(006)
(110)
(113)
(202)
(018)+(116)
(122)

Figure 2

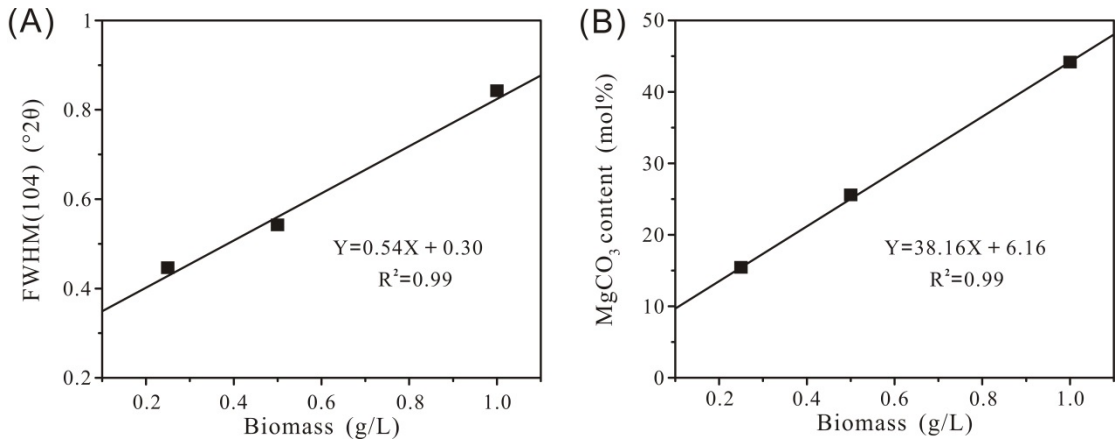
(A)
FWHM(104) (°2θ)
Biomass (g/L)
Y=0.54X + 0.30
R²=0.99
(B)
MgCO3 content (mol%)
Biomass (g/L)
Y=38.16X + 6.16
R²=0.99

Figure 3

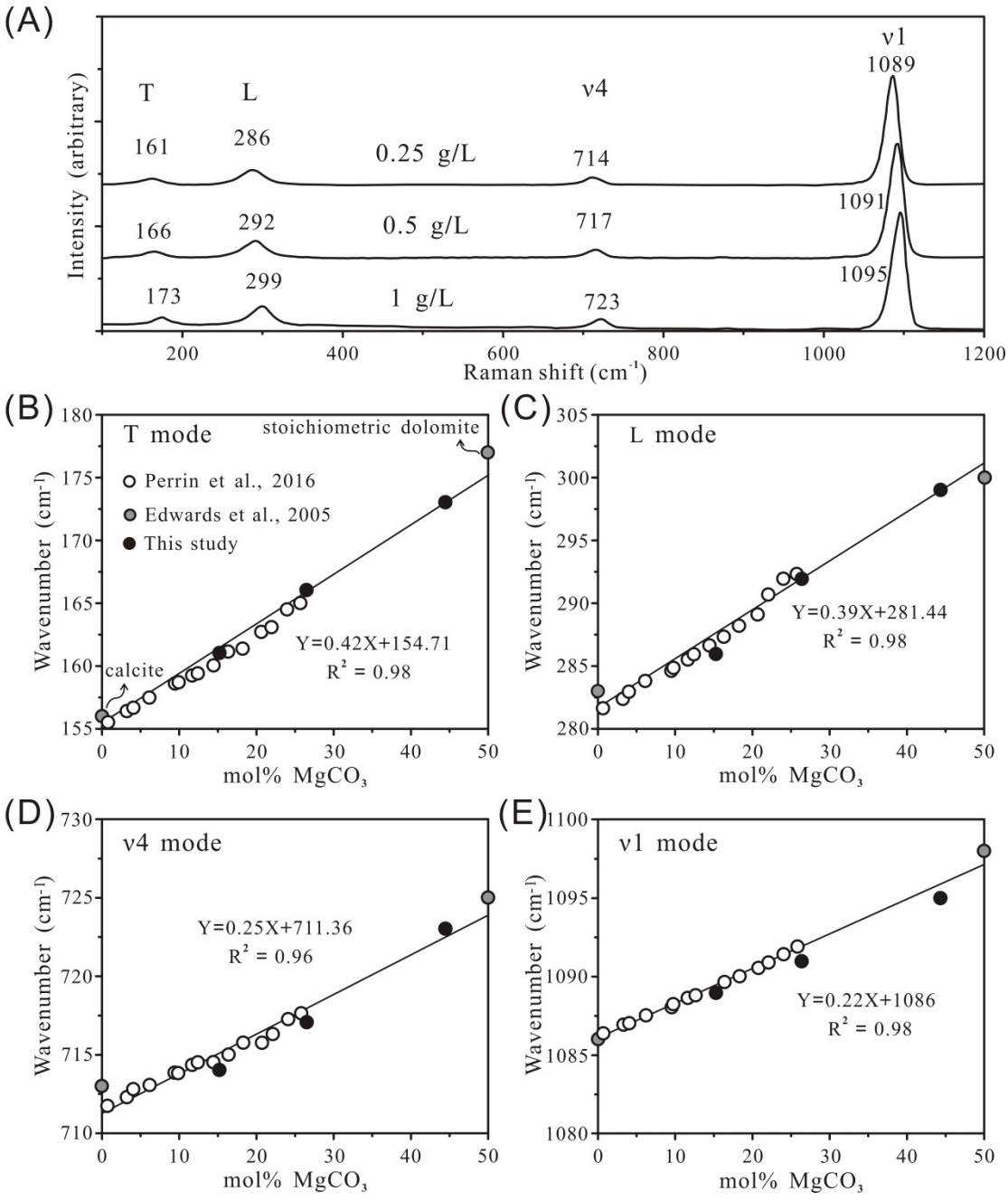
(A)
Intensity (arbitrary)
T
L
ν4
ν1
1089
161
286
0.25 g/L
714
1091
166
292
0.5 g/L
717
1095
173
299
1 g/L
723
200
400
600
800
1000
1200
Raman shift (cm-1)
(B)
T mode
stoichiometric dolomite
Perrin et al., 2016
Edwards et al., 2005
This study
Y=0.42X+154.71
R2 = 0.98
calcite
Wavenumber (cm-1)
mol% MgCO3
(C)
L mode
Y=0.39X+281.44
R2 = 0.98
(D)
ν4 mode
Y=0.25X+711.36
R2 = 0.96
(E)
ν1 mode
Y=0.22X+1086
R2 = 0.98

Figure 4

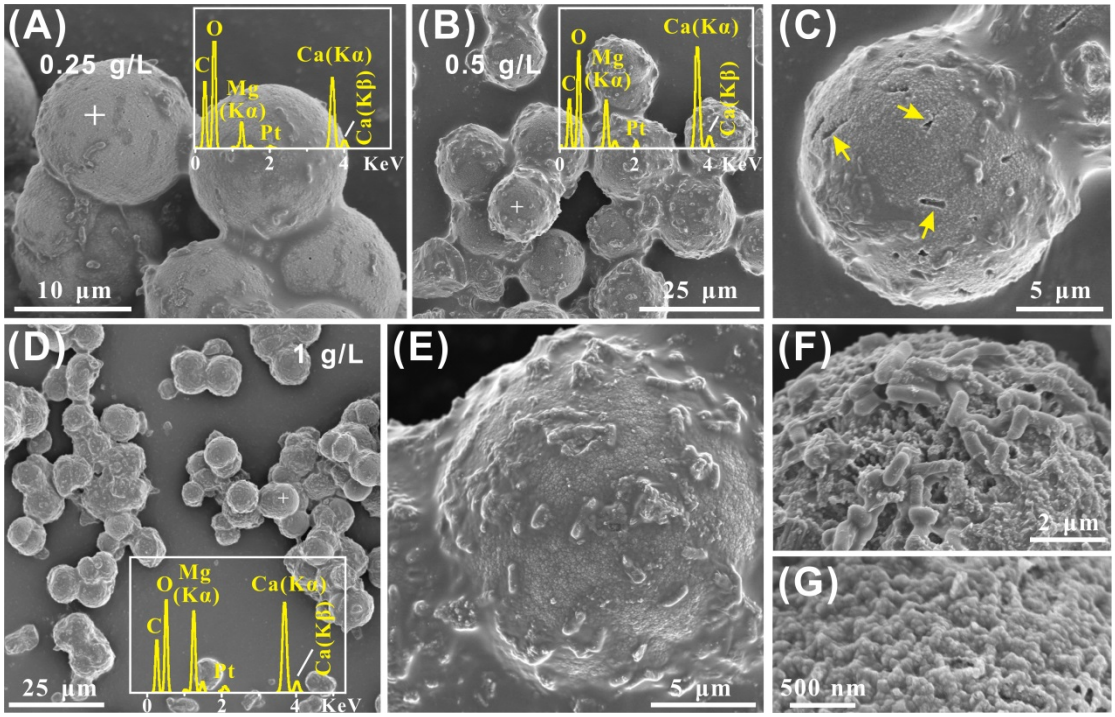
(A)
0.25 g/L
O
C
Mg (Kα)
Pt
Ca(Kα)
Ca(Kβ)
0
2
4 KeV
10 μm
(B)
0.5 g/L
O
C
Mg (Kα)
Pt
Ca(Kα)
Ca(Kβ)
0
2
4 KeV
25 μm
(C)
5 μm
(D)
1 g/L
O
C
Mg (Kα)
Pt
Ca(Kα)
Ca(Kβ)
0
2
4 KeV
25 μm
(E)
5 μm
(F)
2 μm
(G)
500 nm

Figure 5

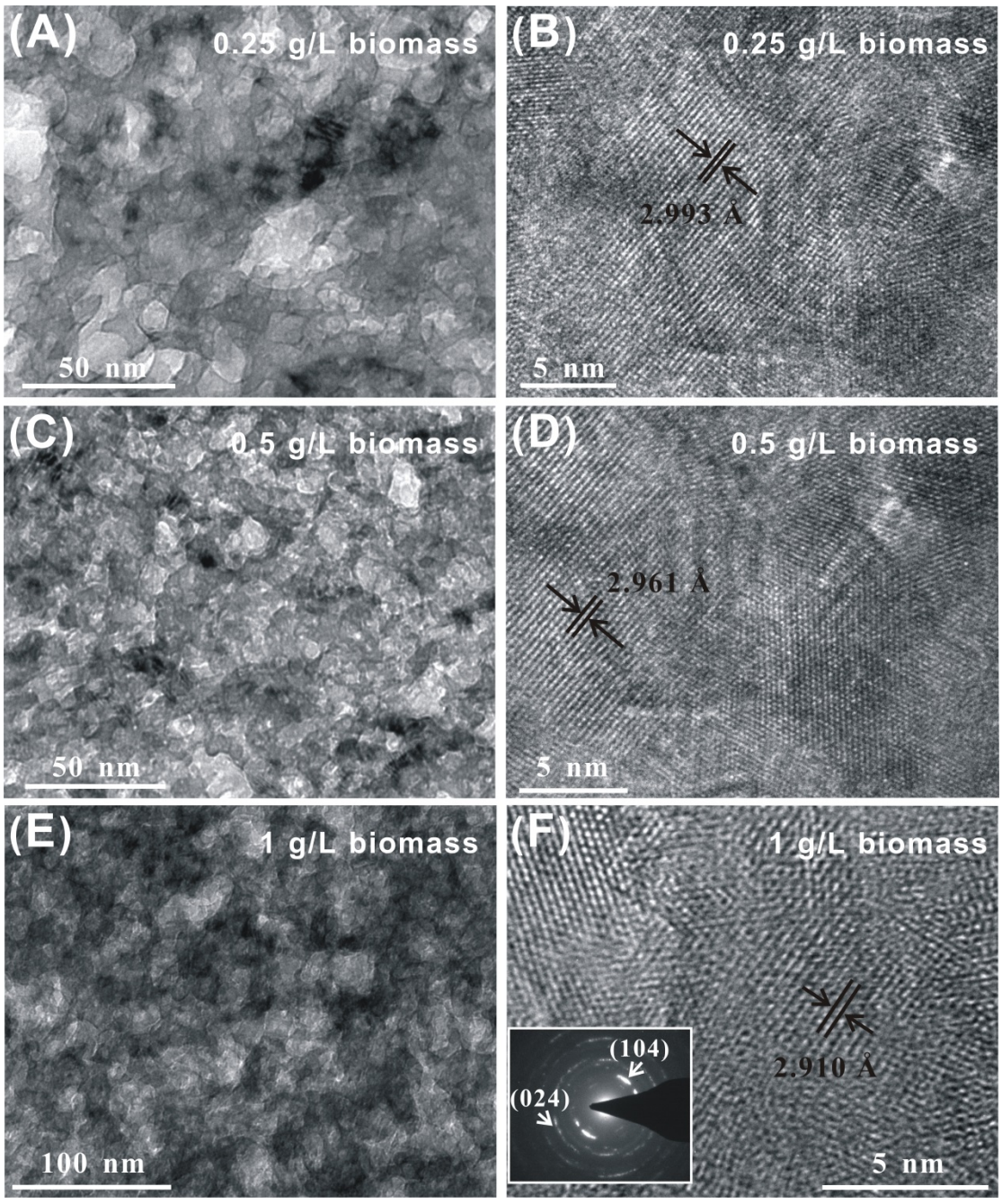
(A)
0.25 g/L biomass
50 nm
(B)
0.25 g/L biomass
2.993 Å
5 nm
(C)
0.5 g/L biomass
50 nm
(D)
0.5 g/L biomass
2.961 Å
5 nm
(E)
1 g/L biomass
100 nm
(F)
1 g/L biomass
(104)
(024)
2.910 Å
5 nm

Figure 6

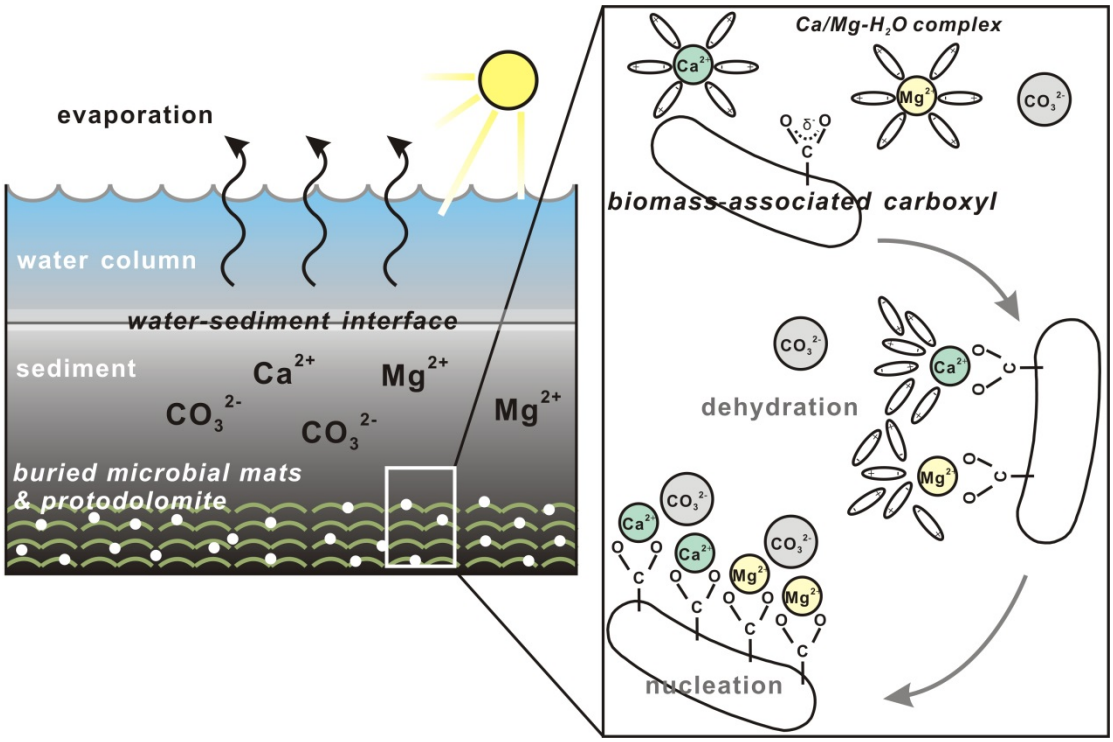
evaporation
water column
water-sediment interface
sediment
Ca2+
Mg2+
CO3 2-
CO3 2-
Mg2+
buried microbial mats
& protodolomite
Ca/Mg-H2O complex
biomass-associated carboxyl
dehydration
nucleation

Figure 7